Multi-resolution dataset for photovoltaic panel segmentation from satellite and aerial imagery

Hou Jiang[1], Ling Yao[1,2,3,*], Ning Lu[1,2,3], Jun Qin[1,2], Tang Liu[4], Yujun Liu[1,5], Chenghu Zhou[1]

[1]State Key Laboratory of Resources and Environmental Information System, Institute of Geographic Sciences and Natural Resources Research, Chinese Academy of Sciences, Beijing, 100101, China

[2]Southern Marine Science and Engineering Guangdong Laboratory, Guangzhou 511458, China

[3]Jiangsu Center for Collaborative Innovation in Geographical Information Resource Development and Application, Nanjing Normal University, Nanjing 210023, China

[4]School of Information Engineering, China University of Geosciences (Beijing), Beijing, 100083, China

[5]Provincial Geomatics Center of Jiangsu, Nanjing, 210013, China

Correspondence to: Ling Yao (yaoling@lreis.ac.cn)

Abstract. In the context of global carbon emission reduction, solar photovoltaics (PV) is experiencing rapid development. Accurate localized PV information, including location and size, is the basis for PV regulation and potential assessment of energy sector. Automatic information extraction based on deep learning requires high-quality labelled samples that should be collected at multiple spatial resolutions and under different backgrounds due to the diversity and variable scale of PV. We established a PV dataset using satellite and aerial images with spatial resolutions of 0.8m, 0.3m and 0.1 m, which focus on concentrated PV, distributed ground PV and fine-grained rooftop PV, respectively. The dataset contains 3716 samples of PVs installed on shrub land, grassland, cropland, saline-alkali, and water surface, as well as flat concrete, steel tile, and brick roofs. The~~We used this~~ dataset is used to examine the model performance of different deep networks on PV segmentation. O~~, and o~~n average, an intersection over union (IoU) greater than 85% i~~wa~~s achieved. In addition, our experiments show that direct cross application between samples with different resolutions is not feasible, and that fine-tuning of the pre-trained deep networks using target samples is necessary. The dataset can support more works on PVs for greater value, such as, developing PV detection algorithm, simulating PV conversion efficiency, and estimating regional PV potential. The dataset is available from Zenodo on the following website: https://doi.org/10.5281/zenodo.5171712 (Jiang et al. 2021).

1 Introduction

Fossil fuels used by our society have caused unprecedented levels of carbon dioxide (CO_2), with widespread climate impacts that threaten human survival and development (Chu and Majumdar 2012; Shin et al. 2021). Therefore, governments around the world intensively made commitments to reduce greenhouse gas emissions and formulated schedules for carbon peak and neutrality. For example, the U.S. government announced the goal of achieving carbon neutrality by 2050, and the Chinese government promised to achieve carbon peak by 2030 and carbon neutrality by 2060. To achieve this, a variety of techniques

31 have been developed to generate electricity from renewable energy sources (Moutinho and Robaina 2016), of which solar

32 energy has attracted increasing attention because of its endless availability and environmental friendliness (Kabir et al. 2018).

33   The photovoltaic (PV) market has experienced rapid growth over the past two decades owing to the reduced cost of

34 PV modules and support programs from governments (La Monaca and Ryan 2017; Yan et al. 2019). Between 2000 and 2020,

35 worldwide installed capacity increased from 4 GW to 714 GW, consistently exceeding expectations (IRENA 2021). Utility-

36 scale PV plants usually need large ground installation area, thusand face the land use competition with other human activities

37 (Majumdar and Pasqualetti 2019; Sacchelli et al. 2016). Adverse impacts regarding the availability of land resources and

38 land erosion are encountered in PV installed regions (Hernandez et al. 2015; Rabaia et al. 2021), which encourages regular

39 monitoring of PV plants during their working lifetime. Distributed solar PVs are installed on marginal agricultural lands

40 (Martins et al. 2007), building rooftops (Bódis et al. 2019), water surfaces (Liu et al. 2019), and other unused lands, to

41 minimize potential ecological and environmental impacts. In contrast to utility-scale PVs, distributed PVs generate power in

42 isolation; hence, it is necessary to adopt grid-connected technology to integrate them into electrical networks for achieving

43 the greatest benefits (Zambrano-Asanza et al. 2021). To help with PV integration and monitoring, there are strong interests

44 among governments and utility decision-makers in obtaining localized information of existing PVs, such as the location,

45 size, capacity, and power output (Rico Espinosa et al. 2020; Yao and Hu 2017). Traditional methods, such as in-situ survey

46 and bottom-up reporting, are generally time-consuming and incomplete. In addition, the obtained results lack the desired

47 geospatial precision, and may be outdated due to the rapid growth of PVs. Therefore, frequent data collection is necessary,

48 and efficient data acquisition method is required.

49   With the advance of spatio-temporal resolution of on-board sensors, satellite and aerial photography can provide

50 up-to-date images of specific ground targets, making them an ideal source for obtaining accurate PV information (Perez et al.

51 2001; Peters et al. 2018; Wang et al. 2018). PV panels can be detected and segmented from satellite or aerial images by

52 designing representative features (e.g., color, spectrum, geometry, and texture). However, these features vary with different

53 atmospheric conditions, light circumstances, satellite sensors, observation scales, and surroundings, leading to the defects of

54 generalization ability in extended applications (Ji et al. 2019; Ji et al. 2020; Wang et al. 2018). Deep learning is favoured in

55 recent years in view of its success in object detection and image classification. Several convolutional neural networks

56 (CNNs) have been proposed to localize solar PVs from satellite imagery and estimate their sizes (Golovko et al. 2017; House

57 et al. 2018; Liang et al. 2020; Malof et al. 2015). For example, Yu et al. (2018) utilized the transfer learning to train a CNN

58 classifier for PV identification, then added an additional CNN branch directly connected to the intermediate layers for PV

59 segmentation. Apart from the structure of deep networks, the quality of labelled samples largely determines the final

60 accuracy of obtained information (Ball et al. 2017; Reichstein et al. 2019). Researchers have spent a huge amount of time on

61 building benchmark datasets generated from aerial or satellite imagery (Ji et al. 2019; Li et al. 2020; Xia et al. 2018).

62 However, to date, there are no open-source datasets available for PVs, and no relevant studies evaluating the generalization

63 ability of deep learning from aerial data to satellite data, and vice versa.

64   To meet the requirements of deep learning for labelled samples, we built a PV dataset from satellite and aerial

65   imagery ~~with~~ at three different spatial resolutions (i.e., 0.8m, 0.3m and 0.1m). We tested the effectiveness of our datasets in

66   extracting multi-scale PVs using the coarse satellite samples (0.8m) for concentrated PVs, the medium aerial samples (0.3m)

67   for distributed ground PVs, and the high-resolution unmanned aerial vehicle (UAV) samples (0.1m) for fine-grained rooftop

68   PVs. In addition, we evaluated the feasibility of deep networks for cross applications between satellite and aerial samples.

69   Our dataset will contribute to a variety of PV applications in the future.

70   **2 Sampling area and data sources**

71   All PV samples are collected in Jiangsu province, China, covering a total area of 107,200 square kilometres (Fig. 1a).

72   Located in the lower reaches of the Yangtze River and Huaihe River, the province is very flat, averaging only 12.3m above

73   sea level. The land terrain is mostly made up of low lands and flat plains, with hills and mountains in the southwest and

74   north (Fig. 1b). With the continuous economic development and population growth, the energy demand in Jiangsu province

75   increases rapidly. The government was committed to energy transition by improving energy efficiency and promoting the

76   use of green energy. A number of policies were introduced to popularize solar PVs. Due to the shortage of land resources,

77   most of installed PVs in Jiangsu province are distributed in areas where land competition is not fierce (e.g., sparse shrubs,

78   low-density grasslands, reservoirs, ponds, saline alkali lands and rooftops), which makes it convenient to collect various PVs

79   with different backgrounds.

80   The sizes of distributed PVs typically vary from a few panels to several hectares, depending on the area of available

81   background land. It is difficult to identify all these PVs from a single data source; hence, we used satellite and aerial images

82   with different spatial resolutions to collect PV samples at various scales. Gaofen-2 and Beijing-2 satellite images are used to

83   prepare samples of large-scale PVs. Gaofen-2 is part of the CHEOS (China High Resolution Earth Observation System)

84   family, and is capable of acquiring images with a ground sampling distance (GSD) of 0.81m in panchromatic and 3.24m in

85   multispectral bands. Beijing-2 satellite constellation consists of three satellites, and can provide images with a GSD of 0.80m

86   in panchromatic and 3.2 m in blue, green, red and near infrared bands. Aerial imagery with a GSD of 0.3m is used to collect

87   samples of ground distributed PVs. The aerial photography was conducted by the Provincial Geomatics Centre of Jiangsu in

88   2018, covering the whole Jiangsu province. UAV images are used to collect rooftop PV samples. The UAV flight was

89   carried out in Hai'an County (yellow box in Fig. 1b), where the development of rooftop PVs is relatively mature. Ground

90   control point (GCP) data obtained by continuous operating reference stations were used for georeferencing. The final

91   orthophotos have a GSD of 0.1m and location accuracy of approximately 0.02m. Fig. 1c–d illustrate the appearance of two

92   rooftop PVs in different images. In Gaofen-2 image, the PVs take up only a dozen of pixels that are mixed with surrounding

93   rooftops (Fig. 1c). It is difficult to distinguish the PVs from the background~~s~~, let alone get their exact position and size. In

94   contrast, PV detection becomes slightly easier in the aerial photograph (Fig. 1d), but obtaining accurate PV boundaries is

still difficult. In the UAV image (Fig. 1e), we can clearly recognize the PVs, obtain their boundaries, and even count how many panels each PV is composed of. This example illustrates the necessity of using multi-resolution images to build PV datasets that meet the needs of a variety of applications.
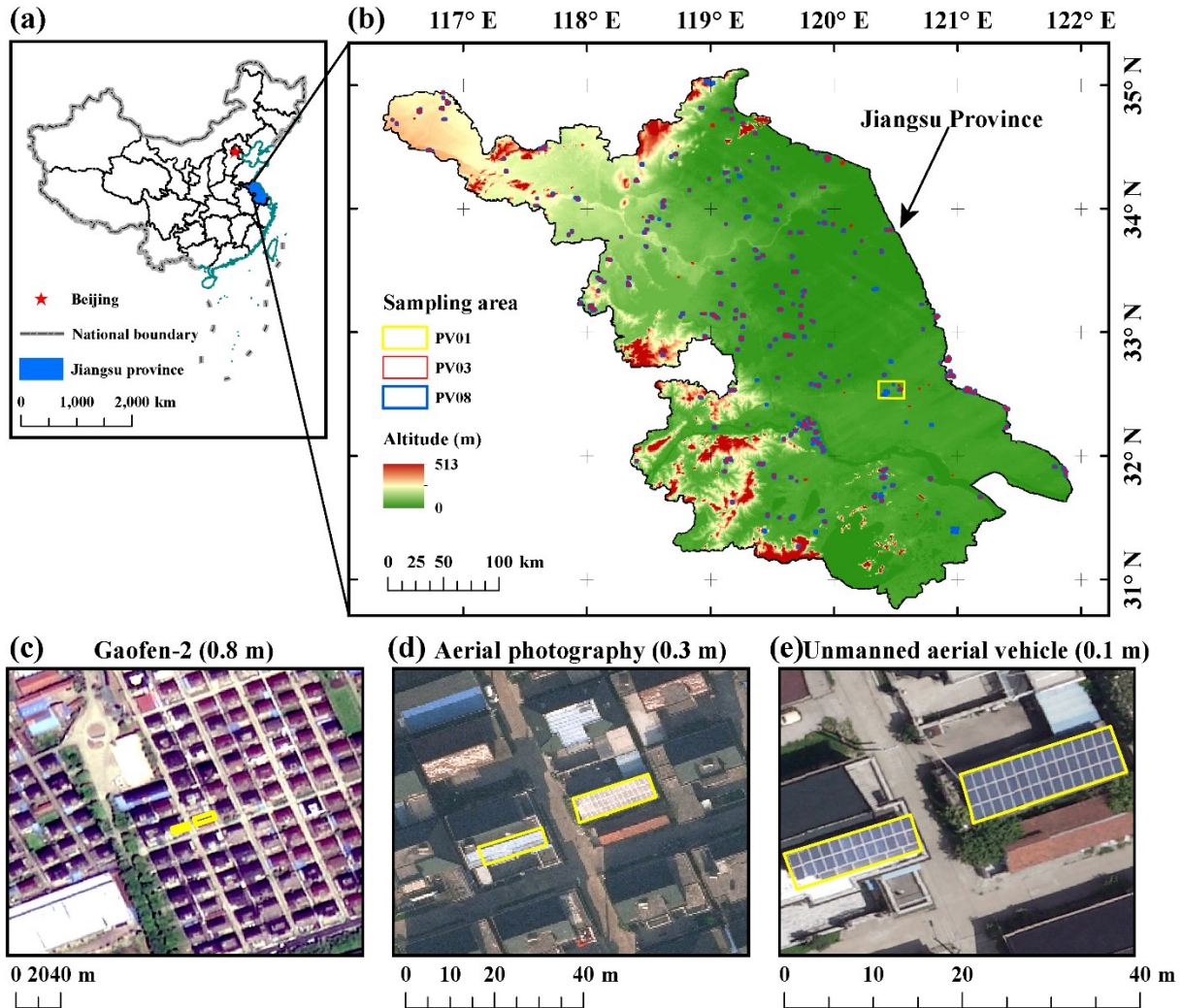
Figure 1: Sampling area and data sources. (a) The location of Jiangsu province in China; (b) spatial distribution of all sampling areas; (c) Gaofen-2 satellite image with a spatial resolution of 0.8m; (d) image from aerial photography with a spatial resolution of 0.3m; and (e) image from unmanned aerial vehicle with a spatial resolution of 0.1m. The yellow boxes in sub-figure (c-e) represent the same rooftop PVs.

3 Generation of PV samples

The schematic workflow to generate PV samples is shown in Fig. 2. The main procedures are described in the following:

1) *Data pre-processing*. To obtain high-quality PV samples, a series of pre-processing methods were applied to the original satellite and aerial images. We first checked the raw data and removed images with lots of clouds, noise and bright spots. Geometric correction was undertaken to eliminate the spatial distortions in original images, and additional ortho-rectification was used for aerial images to minimise the perspective (tilt) and relief (terrain) effects. The adaptive Pan sharpening method (Song et al. 2016) was utilized to improve the spatial resolution of multi-spectral images by fusing the panchromatic band. We also performed block adjustment on multi-temporal images to ensure that they have the same location accuracy. Finally, we use histogram equalization to adjust the hue component of the images.

2) ~~Category design~~*Sample organization*. Our PV dataset includes three groups of PV samples collected at different spatial resolutions (Table 1), namely PV08 from Gaofen-2 and Beijing-2 imagery, PV03 from aerial photography, and PV01 from UAV orthophotos. PV08 contains rooftop and ground PV samples. Ground samples in PV03 are divided into five categories according to their background land use type: shrub land, grassland, cropland, saline-alkali, and water surface. Rooftop samples in PV01 are divided into three categories according to their background roof type: flat concrete, steel tile, and brick.

3) *Image annotation*. Due to the differences in the shape, size, and direction of various PVs, we used polygonal annotations, that is, drawing lines by placing points around the outer edges of each PV panel. The inner space surrounded by the points was then assigned a predefined code in Table 1 to indicate the category to which it belongs. The annotators worked in pairs to ensure that each PV panel was annotated twice. After getting the initial annotations, a third annotator would merge the two annotations and check one by one to fix the potential errors. Finally, a supervisor was responsible for checking the quality of all annotations, including location and category. Figure 3 shows some examples of PV panels and their annotations.

4) *Sample making*. The shapefile of polygonal annotations was converted to a raster that has the same spatial resolution as satellite or aerial images. The raster and original red, green and blue (RGB) images were then seamlessly cropped into tiles at a fixed size by referring to the sampling grids. Tiles containing a single category of PV were paired with corresponding image blocks to form a complete sample (refer to the example in Fig. 2). We prepared PV08 and PV03 samples at the size of 1024×1024 pixels, while PV01 samples at the size of 256×256 pixels. The numbers of each category are listed in Table 1.

One concern of our data set is the representativeness of the samples because the changes in geographic context will inevitably affect the performance of deep learning models. We compared the samples from Gaofen-2 and Beijing-2 images, and found that PV panels exhibit similar characteristic in high-resolution imagery and that the main difference comes from the background. Therefore, we collected samples covering as many backgrounds as possible to ensure the representativeness. Besides, some skills (e.g., transferring learning, cross-domain feature representation) in the deep learning community can be adopted to enhance the generalization ability of deep networks trained by our dataset, which is beyond the discussion of this study. In the following, we introduce some applications of deep learning to illustrate the quality and value of our dataset.
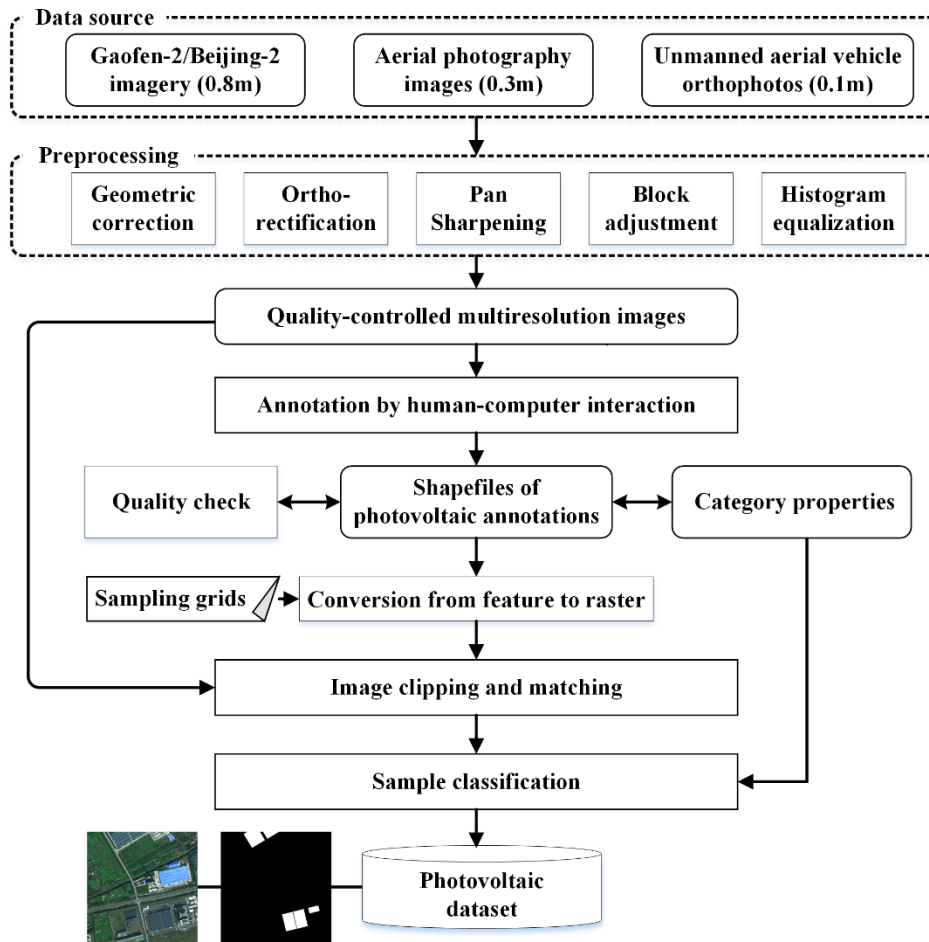
135

136 **Figure 2: Flowchart to generate PV samples.**

137 **Table 1: Organizational structure<s>Classification system</s> of our PV dataset.**

Dataset	Category	Spatial Resolution	Code	Size	Num.
PV08	PV08_Rooftop	~0.8m	11	1,024×1,024	90
	PV08_Ground	~0.8m	12	1,024×1,024	673
PV03	PV03_Rooftop	~0.3m	111	1,024×1,024	236
	PV03_Ground_Shrubwood	~0.3m	121	1,024×1,024	119
	PV03_Ground_Grassland	~0.3m	122	1,024×1,024	117
	PV03_Ground_Cropland	~0.3m	123	1,024×1,024	859
	PV03_Ground_SalineAlkali	~0.3m	124	1,024×1,024	352
	PV03_Ground_WaterSurface	~0.3m	125	1,024×1,024	625
PV01	PV01_Rooftop_FlatConcrete	~0.1m	211	256×256	413
	PV01_Rooftop_SteelTile	~0.1m	212	256×256	94
	PV01_Rooftop_Brick	~0.1m	213	256×256	138

138
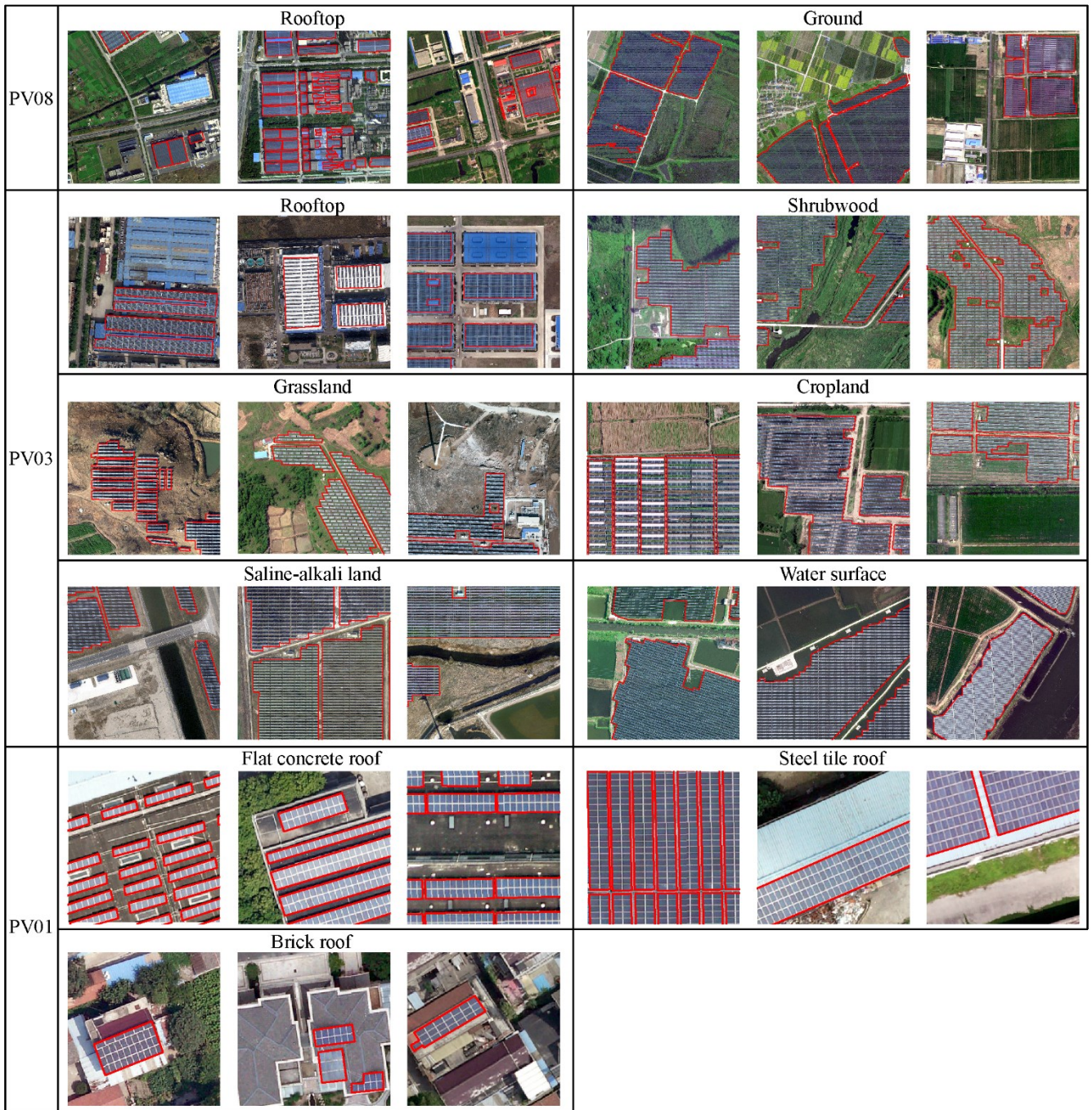
Figure 3: Examples of PV panels and their annotations. Red boxes indicate ~~are the manually drawn~~the -boundaries of PV panels.

139

4 Applications of the dataset

4.1 PV segmentation using deep networks

To examine the possibility of extracting multi-scale PVs from complex backgrounds based on our dataset, we carried out a group of segmentation experiments using deep learning. We compared the performance of three deep networks, including U-Net (Ronneberger et al. 2015), RefineNet (Lin et al. 2017) and DeepLab v3+ (Chen et al. 2018). The U-Net consists of a contracting path (encoder) to capture context and a symmetric expanding path (decoder) that enables precise localization. The feature map of the encoder is combined with the up-sampling feature map of the decoder through skip connection to generate final segmentation map. The RefineNet is a multi-path refinement network, which exploits all information available along the down-sampling process to enable high-resolution prediction. The high-level semantic features are refined using low-level fine-grained features. In addition, a chained residual pooling is introduced into individual residual connections to capture background context. The DeepLab v3+ combines the advantages from spatial pyramid pooling module and encode-decoder structure. The former is capable of encoding multi-scale contextual information, while the latter can enhance the ability to capture object boundaries.

The experiments were conducted on PV08, PV03 and PV01 dataset ~~dataset~~, respectively. For each sub-category (e.g., PV08_Rooftop, PV08_Ground), all samples were separated into 80% training set (from which 20% samples were used for validation) and 20% testing set. The Adam optimizer was used for training and an early-stopping mechanism was adopted to prevent overfitting. The final segmentation results were evaluated using five indicators, including accuracy, precision, recall, F1 score, and intersection over union (IoU). Accuracy refers to the ratio of PV and background correctly classified by the model to the sum of PV and background in the image. Precision is the ratio of PV correctly identified by the model to the total PV identified by the model, describing the reliability of PV segmentation results. The recall equals the ratio of PV correctly identified by the model to the actual total PV. F1 score ($\frac{2 \times \text{precision} \times \text{recall}}{\text{precision} + \text{recall}}$) is a weighted average of precision and recall, providing a comprehensive evaluation of PV extraction results. IoU is the ratio of the intersection to the union between PV identified by the model and the actual PV. The evaluation accuracy of PV segmentation results is summarized in Table 2. It is noted that different networks were compared under equal conditions, and additional techniques (e.g., data augmentation, class weight) were not taken into account.

Overall, DeepLab v3+ achieved the highest accuracy across all three datasets, followed by RefineNet and U-Net. The disparity among different models was relatively small at coarse spatial resolution (approximately 2% in terms of IoU), but the advantage of complex network became obvious as the spatial resolution increases (IoU difference reaches 5% for PV03 and 8% for PV01). The reasonable explanation is that in coarse satellite images the blurred boundaries between PV and background prevent the complex networks from acquiring more useful information. Figs. 4–6 show some examples, which helps in understanding the effects of network structure and image resolution on the final segmentation results. With respect to the results of DeepLab v3+, some parts of PV were lost (e.g., Figs. 4d, 5d and 6c) and the gaps between adjacent

172 PVs were wider than the actual (e.g., Figs. 4b, 5d and 6b). In contrast, RefineNet and U-Net misclassified portions with
173 similar characteristics as PV (e.g., Figs. 4a, 4b, 4d, 5a, 5c, 5f, 6b and 6c). The phenomena suggest that DeepLab v3+ tends to
174 ensure the extracted PVs are reliable, while RefineNet and U-Net try to identify all PVs as many as possible. This explains
175 why the precision of DeepLab v3+ was superior to those of RefineNet and U-Net, but the recall was the opposite (Table 2).

176 **Table 2. Segmentation accuracy in terms of different evaluation indices.**

Dataset	Model	Accuracy	Precision	Recall	F1 score	IoU
PV08	U-Net	0.980	0.871	0.864	**0.868**	0.776
	RefineNet	0.979	0.848	**0.884**	0.866	0.773
	DeepLab v3+	**0.984**	**0.877**	0.857	0.867	**0.790**
PV03	U-Net	0.973	0.897	0.935	0.916	0.858
	RefineNet	0.976	0.957	**0.937**	**0.947**	0.878
	DeepLab v3+	**0.983**	**0.959**	0.931	0.945	**0.908**
PV01	U-Net	0.961	0.831	**0.900**	0.864	0.787
	RefineNet	0.981	0.909	0.897	0.903	0.859
	DeepLab v3+	**0.983**	0.928	0.894	**0.911**	**0.868**
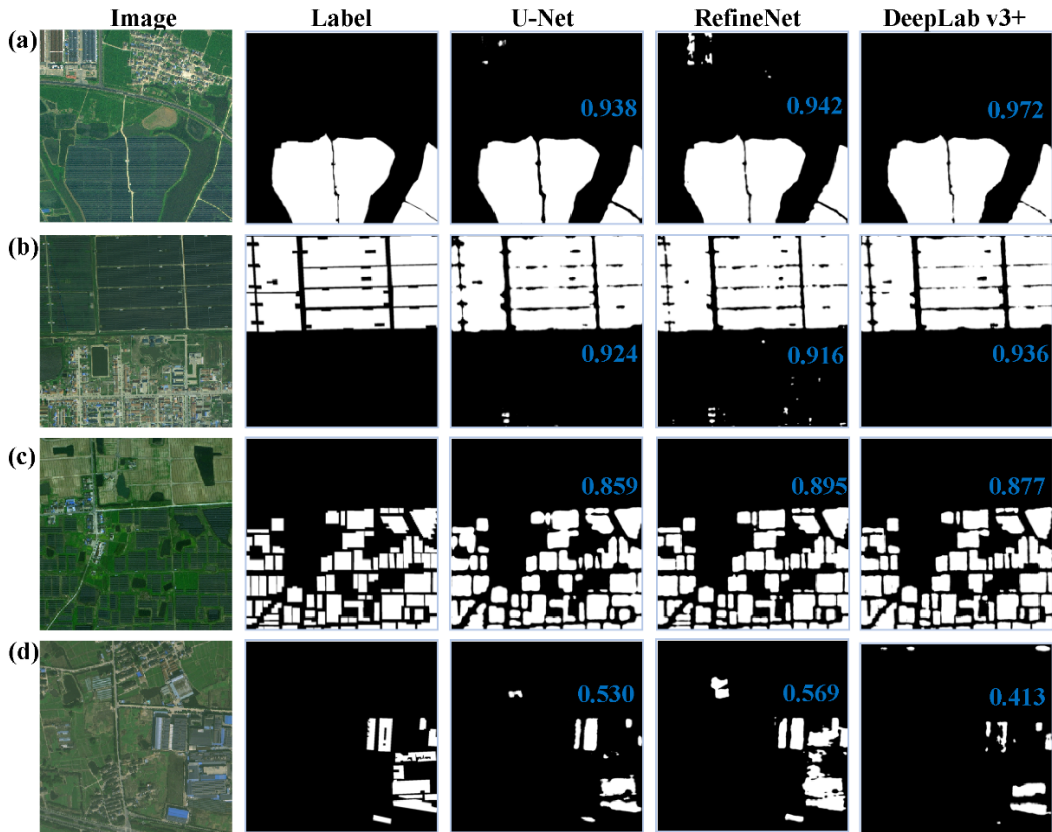
177

178 **Figure 4: Segmentation results of PVs in PV08 dataset. We show examples of concentrated ground PVs (a, b), distributed ground**
179 **PV (c), and distributed rooftop PV (d). IoU of each segmentation result is marked in blue within the image.**

180
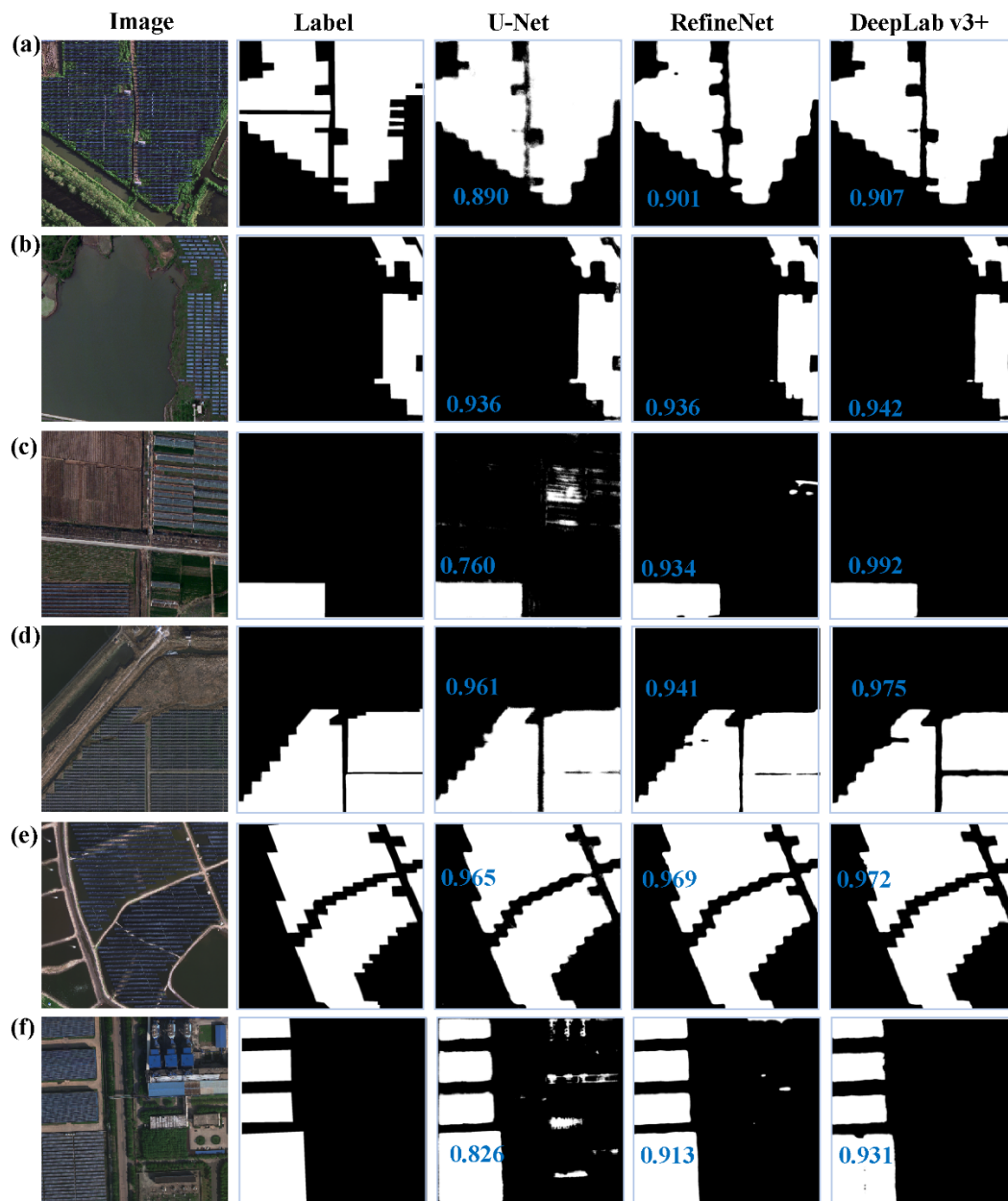
Figure 5: Segmentation results of PVs in PV03 dataset. Examples correspond to PV on shrub land (a), grassland (b), cropland (c), saline-alkali (d), water surface (e), and rooftop (f), respectively. IoU of each segmentation result is marked in blue within the image.

184
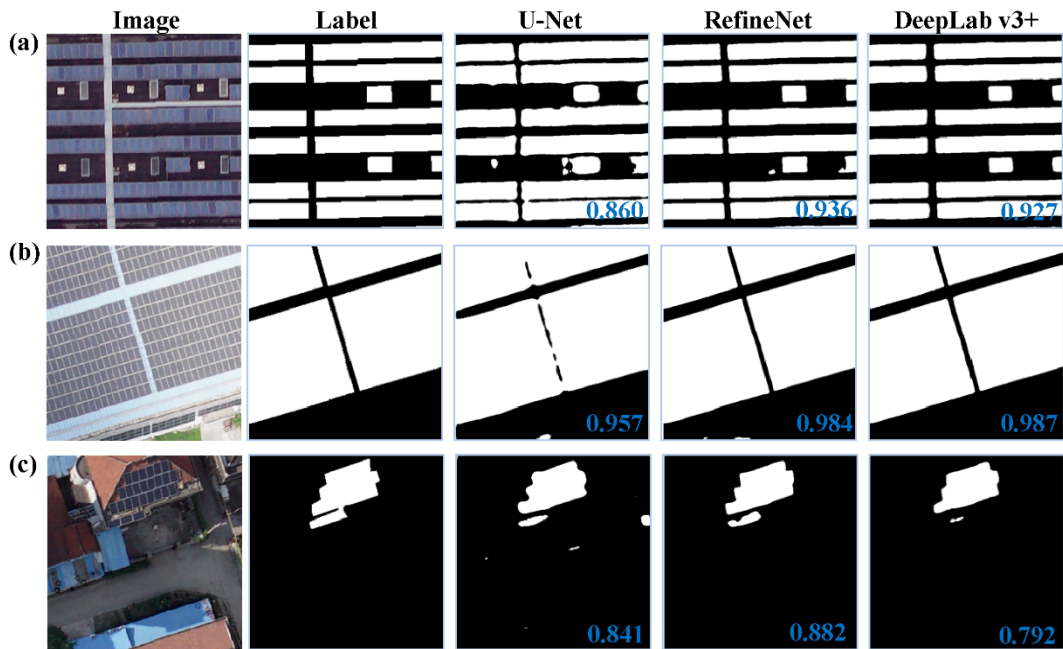
Figure 6: Segmentation results of PVs in PV01 dataset. Examples corresponds to PV on flat concrete (a), steel tile (b) and brick (c) roofs, respectively. IoU of each segmentation result is marked in blue within the image.

Utility-scale PVs account for approximately 88% of the samples in PV08. The unbalance of training samples led to the difference in segmentation accuracy (higher for utility-scale PVs while lower for distributed PVs, Fig. 4). Except that, the spatial resolution was responsible for the poor performance on distributed PVs (Fig. 4c–d) that were mixed with background in the 0.8m satellite images. We may conclude that PV08 samples are only suitable for large-scale PV extraction, and higher resolution is required for distributed PVs. Intuitively, the texture of distributed PV becomes clear in the 0.3m aerial images, and the contrast to background is significant, making it easy to distinguish PV from various backgrounds. The average IoU of DeepLab v3+ reached 0.900, 0.884, 0.920, 0.903, 0.911, and 0.926 for PVs on shrub land, grassland, cropland, saline-alkali, water surface, and rooftop, respectively, which revealed that the segmentation accuracy was slightly affected by the background land types. PVs on flat concrete and steel tile roofs occupy the entire roof of large buildings, such as factories, shopping malls, business centres and urban residential buildings, thus seem "large-scale" in the UAV images with a spatial resolution of 0.1 m. On average, DeepLab v3+ achieved an IoU of 0.873 for flat concrete PVs and 0.927 for steel tile PVs. In contrast, PVs on brick roofs of rural residential building and urban villa usually consist of several panels because the limited area available for PV installations. These "small-scale" PVs may share the same feature with surrounding roofs or shadows, thus the segmentation accuracy was reduced to 0.850 in terms of IoU. Based on the above analysis, we recommend PV08 for extracting concentrated PVs, PV03 for ground distributed PVs, and PV01 for rooftop distributed PVs.

4.2 Cross application at different resolutions

204 The generalization capability of deep learning is critical to automatic information extraction. This section investigates the
205 feasibility of cross application between PV samples with different spatial resolutions, including between PV08_Ground and
206 PV03_Ground, and between PV03_Rooftop and PV01_Rooftop. We compared the segmentation results of DeepLab v3+
207 from direct training, cross application and fine-tuning. Taking the experiment between PV08_Ground and PV03_Ground as
208 an example, direct training means that DeepLab v3+ trained on PV08 (PV03) samples was applied to PV08 (PV03) samples;
209 cross application means that the model was trained on PV03 (PV08) samples but applied to PV08 (PV03) samples; and fine-
210 tuning means that the model was first pre-trained on PV03 (PV08) samples, then fine-tuned (fine-tuning process lasted 10
211 epochs) using PV08 (PV03) samples, and finally applied to PV08 (PV03) samples. The training set account for 80% of the
212 whole dataset and the testing set is the remaining 20%, but only 20% samples from the training set of the target PV dataset
213 are randomly selected for fine-tuning.

214 According to Table 3, the segmentation accuracy of cross application was terrible with extremely low recall and
215 IoU. After fine tuning, the accuracy increased rapidly to a level comparable to direct training. Some examples are given in
216 Figs. 7–8, where the feature maps indicating the probability that each pixel belongs to PV are illustrated for cross application
217 and fine-tuning experiments. It can be seen that during cross application, the model captured the main feature of PV, but the
218 difference between PV and background was not significant. Through fine-tuning, the differences were enhanced; hence, PV
219 could be easily segmented. Our experiments demonstrate that there are inherent defects in the cross application at different
220 resolutions, but these defects can be compensated by fine-tuning on target dataset. The fine-tuning approach avoids the time
221 consumption of direct training and the huge investment of building ~~compelete~~complete datasets with various resolutions.

222 **Table 3. Segmentation accuracy of DeepLab v3+ trained by different strategies**

Dataset	Model	Accuracy	Precision	Recall	F1 score	IoU
PV08_Ground	Direct training	**0.984**	**0.907**	0.908	**0.908**	**0.845**
	Cross application	0.935	0.856	0.517	0.645	0.492
	Fine tuning	0.978	0.867	**0.922**	0.894	0.823
PV03_Ground	Direct training	**0.981**	**0.960**	**0.903**	**0.931**	**0.877**
	Cross application	0.752	0.726	0.185	0.295	0.177
	Fine tuning	0.975	0.943	0.897	0.919	0.865
PV03_Rooftop	Direct training	0.977	0.824	**0.823**	0.824	0.707
	Cross application	0.894	0.414	0.048	0.086	0.045
	Fine tuning	**0.981**	**0.891**	0.811	**0.849**	**0.747**
	Direct training	**0.983**	**0.928**	**0.894**	**0.911**	**0.868**
PV01_Rooftop	Cross application	0.846	0.672	0.403	0.504	0.368
	Fine tuning	0.965	0.918	0.809	0.860	0.784

223

224
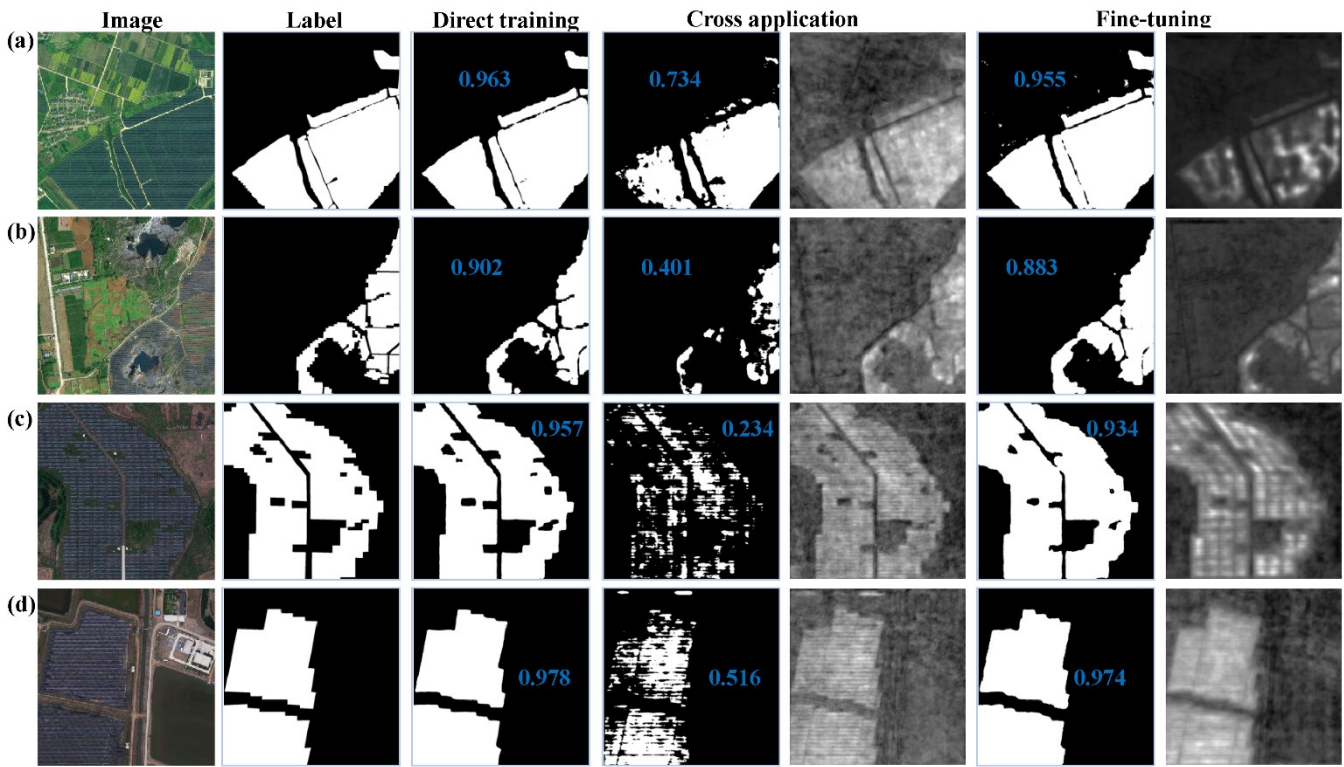
Figure 7: Cross application of ground PV samples. Segmentation results of DeepLab v3+ from direct training, cross application and fine-tuning are shown for PVs in PV08 (a, b) and PV03 (c, d) dataset. Feature map for cross application and fine-tuning is displayed on the right of corresponding segmentation result. IoU of each segmentation result is marked in blue within the image.

228
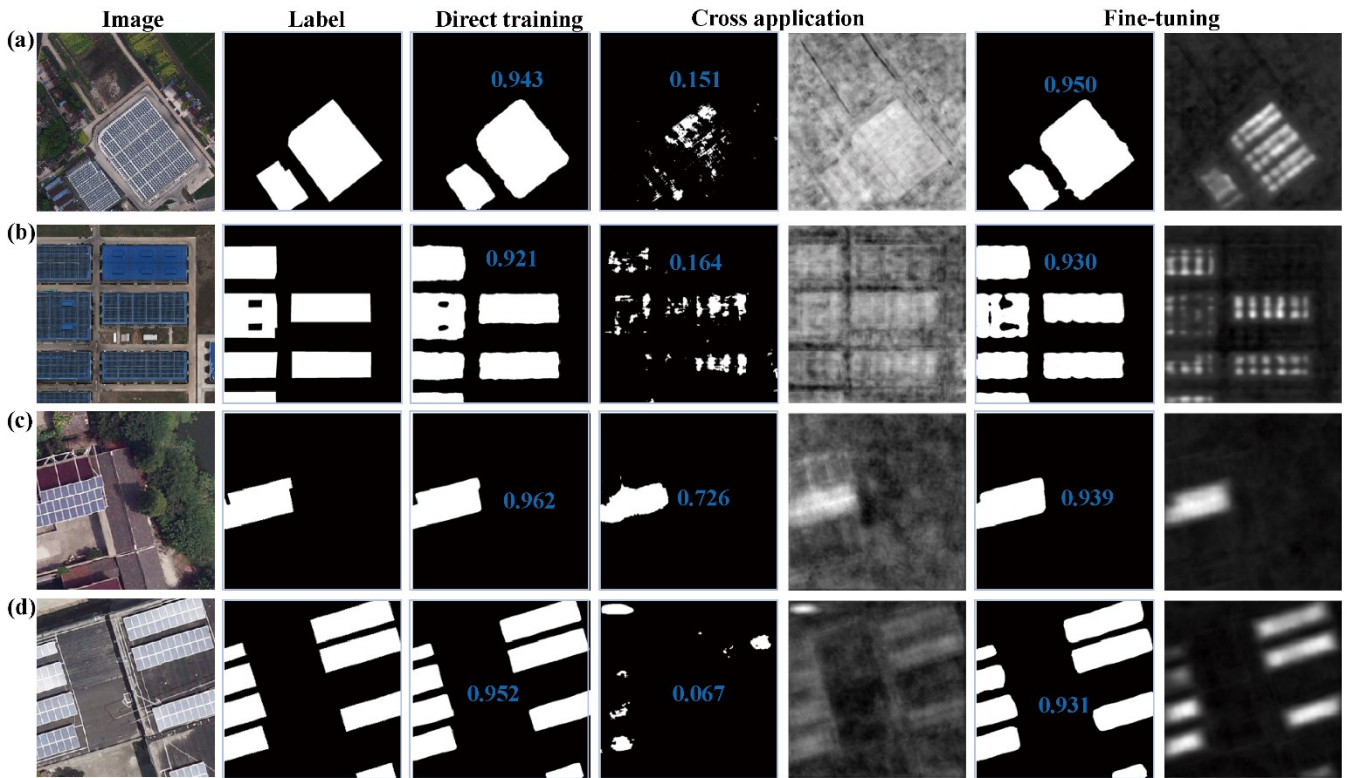
Figure 8: Cross application of rooftop PV samples. Segmentation results of DeepLab v3+ from direct training, cross application and fine-tuning are shown for PVs in PV03 (a, b) and PV01 (c, d) dataset. Feature map for cross application and fine-tuning is displayed on the right of corresponding segmentation result. IoU of each segmentation result is marked in blue within the image.

5 Data availability

The PV dataset is freely available from the Zenodo website at https://doi.org/10.5281/zenodo.5171712 (Jiang et al. 2021). There are three compressed folders, namely PV08.zip, PV03.zip and PV01.zip, for PV samples collected at the spatial resolution of 0.8m, 0.3m and 0.1m, respectively. The original images are named as "PV0*_XXXXXX_YYYYYYY.bmp" and ~~the~~ corresponding labels are named as "PV0*_XXXXXX_YYYYYYY_label.bmp" (* can be the number 8, 3 or 1). The central location (latitude, longitude) of each image equals (XX.XXXX, YY.YYYYY). For each label, "0" indicates the background while the target PV is recorded as the code listed in Table 1.

6 Conclusions

This study built a multi-resolution dataset for PV panel segmentation, including PV08 from Gaofen-2 and Beijing-2 satellite image with spatial resolution of 0.8m, PV03 from aerial images with spatial resolution of 0.3m, and PV01 from UAV images

with spatial resolution of 0.1m. Samples cover a variety of PVs installed on different lands (i.e., shrub land, grassland, cropland, saline-alkali, and water surface) and various rooftops (i.e., flat concrete, steel tile, and brick roofs), ranging in size from dozens of panels to several hectares. To the best of our knowledge, this is the first open PV dataset with multiple spatial resolutions.

Based on the dataset, we investigated the performance of different deep networks on PV segmentation and evaluated the feasibility of cross application between different resolutions. It is recommended to use PV08 for concentrated PV, PV03 for distributed ground PV, and PV01 for distributed rooftop PV so as to achieve the best segmentation results with an IoU of 0.845, 0.871 and 0.868, respectively. It is also proved that direct cross applications do not work well and fine-tuning of pre-trained network using the target samples is essential. Besides, this dataset may contribute to a diversity of other research and applications related to PV. For example, the segmentation networks are generally sensitive to the observational size and shape in the receptive field; hence, it is valuable to quantitatively explore the general guidelines on selecting image resolutions and input sample sizes for PVs with different sizes. Whether a network can be established to combine images with different resolutions to achieve synchronous identification or segmentation of multi-scale PVs is also of great interest.

255 **Author contributions.** Hou Jiang: Methodology, Formal analysis, Writing – original draft. Ling Yao: Conceptualization,
256 Writing – review & editing, Funding acquisition. Ning Lu: Visualization, Writing – review & editing. Jun Qin: Software,
257 Investigation. Tang Liu: Validation, Data Curation. Yujun Liu: Resources, Data Curation. Chenghu Zhou: Supervision,
258 Project administration.

259 **Competing interests.** The authors declare that they have no conflict of interest.

260 **Acknowledgements.** This work was supported by the National Natural Science Foundation of China (No.41771380), and
261 the Key Special Project for Introduced Talents Team of Southern Marine Science and Engineering Guangdong Laboratory
262 (No. GML2019ZD0301). We are grateful to the Provincial Geomatics Center of Jiangsu for their assistance in processing
263 satellite and aerial images, the GitHub user Attila94 for sharing RefineNet code (https://github.com/Attila94/refinenet-
264 keras), and the GitHub user sunlinlin-aragon for sharing DeepLab v3+ code (https://github.com/sunlinlin-
265 aragon/DeepLabV3_Plus-Tensorflow2.0).

266 **References**

267 Bódis, K., Kougias, I., Jäger-Waldau, A., Taylor, N., and Szabó, S.: A high-resolution geospatial assessment of the rooftop
268 solar photovoltaic potential in the European Union, Renew. Sust. Energ. Rev., 114, 109309, doi:10.1016/j.rser.2019.109309,
269 2019.

270 Ball, J.E., Anderson, D.T., and Chan, C.S.: Comprehensive survey of deep learning in remote sensing: theories, tools, and
271 challenges for the community, J. Appl. Remote Sens., 11, 042609, doi:10.1117/1.JRS.11.042609, 2017.

272 Chu, S., and Majumdar, A.: Opportunities and challenges for a sustainable energy future, Nature, 488, 294–303,
273 doi:10.1038/nature11475, 2012.

274 Golovko, V., Bezobrazov, S., Kroshchanka, A., Sachenko, A., Komar, M., and Karachka, A.: Convolutional neural network
275 based solar photovoltaic panel detection in satellite photos, In, 2017 9th IEEE International Conference on Intelligent Data
276 Acquisition and Advanced Computing Systems: Technology and Applications (IDAACS), 14–19,
277 doi:10.1109/IDAACS.2017.8094501, 2017.

278 Hernandez, R.R., Hoffacker, M.K., Murphy-Mariscal, M.L., Wu, G.C., and Allen, M.F.: Solar energy development impacts
279 on land cover change and protected areas, P. Natl. Acad. Sci. USA, 112, 13579, doi:10.1073/pnas.1517656112, 2015.

280 House, D., Lech, M., and Stolar, M.: Using deep learning to identify potential roof spaces for solar panels, In, 2018 12th
281 International Conference on Signal Processing and Communication Systems (ICSPCS), 1–6,
282 doi:10.1109/ICSPCS.2018.8631725, 2018.

283 IRENA: Renewable capacity statistics 2021, International Renewable Energy Agency (IRENA), Abu Dhabi, 2021.

284 Ji, S., Wei, S., and Lu, M.: Fully convolutional networks for multisource building extraction from an open aerial and satellite
285 imagery data set, IEEE T. Geosci. Remote, 57, 574–586, doi: 10.1109/TGRS.2018.2858817, 2019.

286 Ji, S., Zhang, Z., Zhang, C., Wei, S., Lu, M., and Duan, Y.: Learning discriminative spatiotemporal features for precise crop
287 classification from multi-temporal satellite images, Int. J. Remote Sens., 41, 3162–3174,
288 doi:10.1080/01431161.2019.1699973, 2020.

289 Jiang, H., Yao, L., and Liu, Y.: Multi-resolution dataset for photovoltaic panel segmentation from satellite and aerial
290 imagery, In: zenodo, doi:10.5281/zenodo.5171712, 2021.

291 Kabir, E., Kumar, P., Kumar, S., Adelodun, A.A., and Kim, K.-H.: Solar energy: Potential and future prospects, Renew.
292 Sust. Energ. Rev., 82, 894–900, doi:10.1016/j.rser.2017.09.094, 2017.

293 La Monaca, S., and Ryan, L.: Solar PV where the sun doesn't shine: Estimating the economic impacts of support schemes
294 for residential PV with detailed net demand profiling, Energ. Policy, 108, 731–741, doi:10.1016/j.enpol.2017.05.052, 2017.

295 Li, K., Wan, G., Cheng, G., Meng, L., and Han, J.: Object detection in optical remote sensing images: A survey and a new
296 benchmark, ISPRS J. Photogramm., 159, 296–307, doi:10.1016/j.isprsjprs.2019.11.023, 2020.

297 Liang, S., Qi, F., Ding, Y., Cao, R., Yang, Q., and Yan, W.: Mask R-CNN based segmentation method for satellite imagery
298 of photovoltaics generation systems, In, 2020 39th Chinese Control Conference (CCC), 5343–5348,
299 doi:10.23919/CCC50068.2020.9189474, 2020.

300 Liu, L., Sun, Q., Li, H., Yin, H., Ren, X., and Wennersten, R.: Evaluating the benefits of Integrating Floating Photovoltaic
301 and Pumped Storage Power System. Energ. Convers. Manage., 194, 173–185, doi:10.1016/j.enconman.2019.04.071, 2019.

302 Majumdar, D., and Pasqualetti, M.J.: Analysis of land availability for utility-scale power plants and assessment of solar
303 photovoltaic development in the state of Arizona, USA, Renew, Energ., 134, 1213–1231, doi:10.1016/j.renene.2018.08.064,
304 2019.

305 Malof, J.M., Rui, H., Collins, L.M., Bradbury, K., and Newell, R.: Automatic solar photovoltaic panel detection in satellite
306 imagery, In, 2015 International Conference on Renewable Energy Research and Applications (ICRERA), 1428–1431,
307 doi:10.1109/ICRERA.2015.7418643, 2015.

308 Martins, F.R., Pereira, E.B., and Abreu, S.L.: Satellite-derived solar resource maps for Brazil under SWERA project, Sol.
309 Energy, 81, 517–528, doi:10.1016/j.solener.2006.07.009, 2007.

310 Moutinho, V., and Robaina, M.: Is the share of renewable energy sources determining the CO_2 kWh and income relation in
311 electricity generation? Renew. Sust. Energ. Rev., 65, 902–914, doi:10.1016/j.rser.2016.07.007, 2016.

312 Perez, R., Kmiecik, M., Herig, C., and Renné, D.: Remote monitoring of PV performance using geostationary satellites, Sol.
313 Energy, 71, 255–261, doi:10.1016/S0038-092X(01)00050-0, 2001.

314 Peters, I.M., Liu, H., Reindl, T., and Buonassisi, T.: Global prediction of photovoltaic field performance differences using
315 open-source satellite data, Joule, 2, 307–322, doi:10.1016/j.joule.2017.11.012, 2018.

316 Rabaia, M.K.H., Abdelkareem, M.A., Sayed, E.T., Elsaid, K., Chae, K.-J., Wilberforce, T., and Olabi, A.G.: Environmental
317 impacts of solar energy systems: A review, Sci. Total Environ., 754, 141989, doi:10.1016/j.scitotenv.2020.141989, 2021.

318 Reichstein, M., Camps-Valls, G., Stevens, B., Jung, M., Denzler, J., Carvalhais, N., and Prabhat: Deep learning and process
319 understanding for data-driven Earth system science, Nature, 566, 195–204, doi:10.1038/s41586-019-0912-1, 2019.

320 Rico Espinosa, A., Bressan, M., and Giraldo, L.F.: Failure signature classification in solar photovoltaic plants using RGB
321 images and convolutional neural networks, Renew. Energ., 162, 249-256, doi:10.1016/j.renene.2020.07.154, 2020.

322 Sacchelli, S., Garegnani, G., Geri, F., Grilli, G., Paletto, A., Zambelli, P., Ciolli, M., and Vettorato, D.: Trade-off between
323 photovoltaic systems installation and agricultural practices on arable lands: An environmental and socio-economic impact
324 analysis for Italy, Land Use Policy, 56, 90–99, doi:10.1016/j.landusepol.2016.04.024, 2016.

325 Shin, H., Hansen, K.U., and Jiao, F.: Techno-economic assessment of low-temperature carbon dioxide electrolysis, Nat.
326 Sustain., doi:10.1038/s41893-021-00739-x, 2021.

327 Wang, M., Cui, Q., Sun, Y., and Wang, Q.: Photovoltaic panel extraction from very high-resolution aerial imagery using
328 region–line primitive association analysis and template matching, ISPRS J. Photogramm., 141, 100–111,
329 doi:10.1016/j.isprsjprs.2018.04.010, 2018.

330 Xia, G., Bai, X., Ding, J., Zhu, Z., Belongie, S., Luo, J., Datcu, M., Pelillo, M., and Zhang, L.: DOTA: A large-scale dataset
331 for object detection in aerial images, In, 2018 IEEE/CVF Conference on Computer Vision and Pattern Recognition, 3974–
332 3983, doi:10.1109/CVPR.2018.00418, 2018.

333 Yan, J.Y., Yang, Y., Campana, P.E., and He, J.J.: City-level analysis of subsidy-free solar photovoltaic electricity price,
334 profits and grid parity in China, Nat. Energy, 4, 709–717, doi:10.1038/s41560-019-0441-z, 2019.

335 Yao, Y., and Hu, Y.: Recognition and location of solar panels based on machine vision, In, 2017 2nd Asia-Pacific
336 Conference on Intelligent Robot Systems (ACIRS), 7–12, doi:10.1109/ACIRS.2017.7986055, 2017.

337 Zambrano-Asanza, S., Quiros-Tortos, J., and Franco, J.F.: Optimal site selection for photovoltaic power plants using a GIS-
338 based multi-criteria decision making and spatial overlay with electric load, Renew. Sust. Energ. Rev., 143, 110853,
339 doi:10.1016/j.rser.2021.110853, 2021.

340